THE JOURNAL OF PHYSICAL CHEMISTRY C

Article

pubs.acs.org/JPCC

Phonon Thermal Properties of Transition-Metal Dichalcogenides MoS_2 and $MoSe_2$ Heterostructure

Jingchao Zhang,[*,†,‡] Yang Hong,[§] Xinyu Wang,[∥] Yanan Yue,[*,†,⊥] Danmei Xie,[†,⊥] Jin Jiang,[†,⊥] Yangheng Xiong,[†,⊥] and Peisheng Li[#]

[†]Key Laboratory of Hydraulic Machinery Transients, Wuhan University, Ministry of Education, Wuhan, Hubei 430072, China

[‡]Holland Computing Center, University of Nebraska-Lincoln, Lincoln, Nebraska 68588, United States

[§]Department of Chemistry, University of Nebraska-Lincoln, Lincoln, Nebraska 68588, United States

[∥]Department of Mechanical Engineering, The University of Hong Kong, Hong Kong

[⊥]School of Power and Mechanical Engineering, Wuhan University, Wuhan, Hubei 430072, China

[#]Jiangxi Province Key Laboratory of Polymer Preparation & Processing, Shangrao Normal University, Shangrao 334001, China

ABSTRACT: Two prototype transition-metal dichalcogenide (TMDC) materials, MoS_2 and $MoSe_2$, have attracted growing attention as promising 2D semiconductors. The heterostructure created by stacking the 2D monolayers in the out-of-plane direction exhibits peculiar properties that can be utilized in electronic applications. The lateral and flexural phonon transport behaviors in $MoS_2/MoSe_2$ heterobilayer are comprehensively investigated using classical molecular dynamics simulations. In-plane thermal conductivity (κ) and out-of-plane interfacial thermal resistance (R) are calculated by nonequilibrium molecular dynamics (NEMD) and transient pump−probe methods, respectively. Thermal conductivity of $MoS_2/MoSe_2$ bilayer 2D sheet is characterized as 28.8 W/m·K, which preserves the high thermal conductivity of most TMDC materials. The maximum κ reductions of MoS_2, $MoSe_2$, and heterobilayer amount to 83.0, 68.9, and 77.1%, respectively, with increasing temperatures from 100 to 500 K. It is also found that the basal-plane thermal performance of $MoS_2/MoSe_2$ bilayer will not be affected by interfacial interactions, which is important in industrial applications. The predicted out-of-plane flexural phonon conductance results reveal that heat flux runs preferably from MoS_2 to $MoSe_2$ than in the reverse direction.

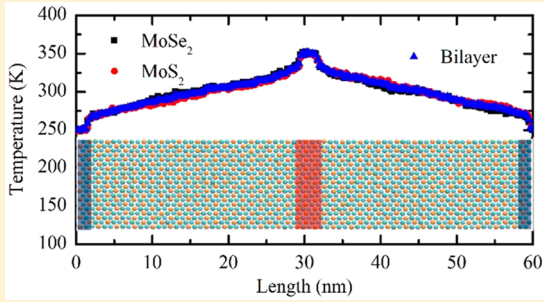

1. INTRODUCTION

Heterostructures play a crucial role in high-speed nanoelectronic and optoelectronic devices and are essential elements in semiconductor industries.[1] Molecular beam epitaxy and epitaxial growth techniques have long been used to fabricate atomic-order thickness heterostructures. However, only limited combinations of materials can be used for good heteroepitaxial growths due to the severe lattice matching conditions restricted by the component materials. The van der Waals (vdW) interfaces have been proven to overcome the obstacle of realizing lattice matching heterostructures.[2] The so-called vdW epitaxy was enabled by stacking different 2D materials into heterobilayers. Because of the weak vdW interaction, the electronic properties can be maintained for individual monolayers. In pursuit of extraordinary 2D materials beyond graphene, enormous attention was given to transition-metal dichalcogenide (TMDC) materials, which exhibit superb thermal and electrical properties.[3−6] Molybdenum disulfide (MoS_2) and molybdenum diselenide ($MoSe_2$) are two prototype semiconductors in the family of TMDCs. Both MoS_2 and $MoSe_2$ show an indirect-gap to direct-gap transition when the system size reduces from bulk to monolayers,[7−9] making it superior to pristine graphene that has no band gap in nanoelectronics applications. The integration of MoS_2 and $MoSe_2$ monolayers into a heterostructure offers the possibility to create devices with peculiar functionalities.[10,11]

The successful synthesis of seamless heterostructures of different TMDCs via chemical vapor deposition (CVD) method has provided an effective solution to produce in-plane $p-n$ junctions, which are critical components in electronic and optoelectronic device applications. Gong et al.[12] used a one-step growth strategy to create WS_2/MoS_2 vertical heterostructures, which exhibited strong localized photoluminescence enhancement and intrinsic $p-n$ junctions. In a similar study, He et al.[13] observed both neutral and charged excitons with large binding energies in the WS_2/MoS_2 bilayer using both experimental and first-principles methods. A prominent voltage-dependent photoresponse was observed in WSe_2/MoS_2 by Son et al.[14] using conductive and photocurrent spectral atomic force microscopy. A relatively lower conductivity is recorded in the lateral junction region because of the energy change in the valence and conduction band edges.

Received: March 17, 2017
Revised: April 25, 2017
Published: May 1, 2017

DOI: 10.1021/acs.jpcc.7b02547
J. Phys. Chem. C 2017, 121, 10336−10344

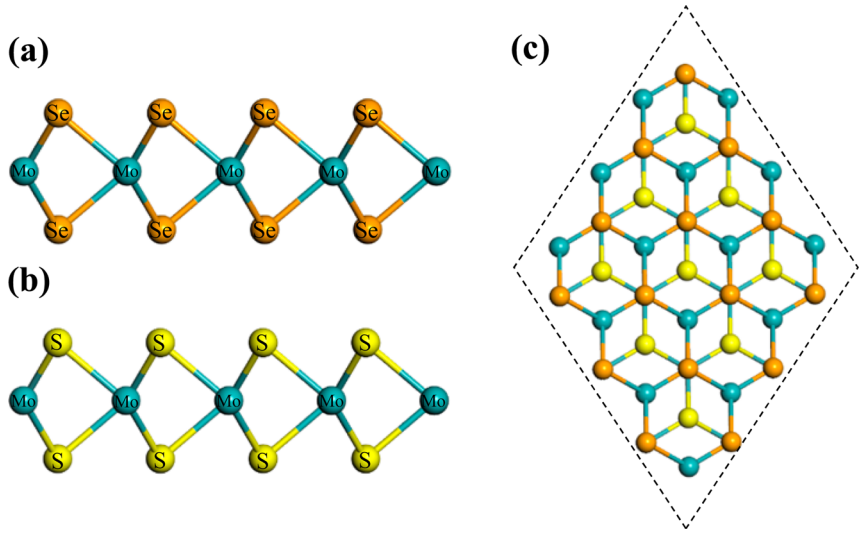

Figure 1. Atomic structures of (a) $MoSe_2$ and (b) MoS_2. Orange, cyan, and yellow solid circles denote Se, Mo, and S atoms, respectively. (c) Top view of the MoS_2−$MoSe_2$ bilayer structure in out-of-plane z direction.

Recently, it has been reported that both the vertical electric field and tensile strain can effectively adjust the bandgaps of $MoS_2/MoSe_2$ bilayers with a lattice mismatch of <5%,[10] making it a promising candidate for optoelectronic applications due to its tunable bandgaps. By employing density functional theory (DFT) computations, Ma et al.[15] investigated heterostructured bilayers of TMDCs. Tunable bandgaps are achieved by manipulating the stretching or compressing pressures, which makes the bilayer structure a promising candidate for electronic device applications. Tang et al.[16] summarizes the recent computational efforts made to reveal the peculiar properties of layered vdW materials, such as hexagonal boron nitride (*h*-BN), MoS_2, and V_2O_5, which further illustrate the importance of TMDC materials in practical applications.

Thermal properties of MoS_2 and $MoSe_2$ have been investigated using both experimental and numerical methods. Yan et al.[17] measured the thermal conductivity of MoS_2 as 34.5 ± 4 W/m·K using Raman thermometry. Suspended and substrate-supported monolayer MoS_2 exhibit similar out-of-plane mode behavior, with differences observed in the in-plane modes resulting from the presence of substrate-induced strain. By solving Boltzmann transport equation, Gandi et al.[18] predicted the thermal conductivity of monolayer MoS_2 as 131 W/m·K at temperature 300 K, which is comparable to that of silicon. Using molecular dynamics method, Hong et al.[19] calculated the thermal conductivity of MoS_2 and $MoSe_2$ as 110.43 and 43.88 W/m·K, respectively, with no anisotropy in armchair and zigzag chiral. Peng et al.[20] predicted thermal conductivity of $MoSe_2$ as 17.6 W/m·K using first-principles calculations. Although the reported results have covered thermal properties of individual MoS_2 and $MoSe_2$ structures, the combined thermal properties for their bilayer heterostructure remain unexplored.

In this work, we studied the phonon transport behavior of $MoS_2/MoSe_2$ bilayer by calculating its lattice thermal conductivity and interfacial thermal resistance using classical molecular dynamics (MD) simulations. We first investigate the dependence of thermal conductivity on crystal size, and extract the bulk thermal conductivity. After that, temperature dependence of thermal conductivity is examined from 100 to 500 K. We also investigate the effect of interlayer coupling strength on predicted in-plane thermal conductivities. The velocity density of state is evaluated to gain a better understanding of the phonon behaviors. Finally, the out-of-plane thermal transport between MoS_2 and $MoSe_2$ is characterized under different temperatures and heat flux directions.

2. MODELING METHODS

For in-plane thermal conductivity characterization, nonequilibrium molecular dynamics (NEMD) method is used with a heat-source placed in the middle and split heat-sinks at two ends. Widths of the heat-source and heat-sink are 2 and 1 nm, respectively. The initial structure is placed in canonical ensemble (*NVT*) for 500 ps (1 ps = 10^{-12} s) to reach steady state at temperature 300 K. Afterward, the simulation system is switched to microcanonical ensemble (*NVE*) for NEMD calculations. Temperature controls in the heat reservoirs are realized by the Langevin thermostat.[21] The thermal energies added to the heat source and extracted from the heat sinks are equal so that the system's total energy conserves. The cumulative energies added/extracted to the atoms are recorded at each time step to calculate the heat fluxes in the monolayers. Thermal energies in MoS_2 and $MoSe_2$ heat reservoirs are recorded separately. The totally added/extracted energy of the bilayer equals the addition of the energies from the monolayers. Another 2.5 ns *NVE* NEMD simulation is performed to build a steady-state temperature gradient. Results from the last 1 ns are used for thermal conductivity characterization. On the basis of Fourier's law of heat conduction, thermal conductivity κ can be calculated from

$$\kappa = -\dot{q}/\nabla T \tag{1}$$

where $\dot{q}$ is heat flux (W/m^2) and ∇T is temperature gradient (K/m). The heat flux $\dot{q}$ is defined as $\dot{q} = J/2A_c$, where J is the added/extracted thermal energy and A_c is the cross-sectional area. It is worth noting that because the heat flux flows in two opposite directions symmetrically, the thermal energy needs to be divided by a factor of 2 for $\dot{q}$ calculations.

When calculating the lateral thermal conductivity of 2D monolayer structures, the material's thickness needs to be selected with great caution. Conventionally, the vdW distance between adjacent layers in the bulk structure is used as the layer

DOI: 10.1021/acs.jpcc.7b02547
J. Phys. Chem. C 2017, 121, 10336−10344

thickness.[22−24] Under such scenario, thickness of MoS_2 d_{MoS_2} is set as 6.1475 Å and thickness of $MoSe_2$ d_{MoSe_2} is 6.469 Å.[19] The overall thickness of the bilayer d_b is the addition of d_{MoS_2} and d_{MoSe_2}, which equals 12.6165 Å. Recently, Wu et al.[25] argued that thickness is not a well-defined quantity for 2D monolayer materials, and thus the same thickness should be used for all 2D materials when comparing their thermal conductivities. The thickness should be regarded as a numerator that needs be unified for fair comparisons of thermal conductivity. Therefore, they used the thickness of graphene 3.35 Å to calculate the heat-transfer capabilities of different 2D materials. To avoid the ambiguous definition of thickness, Wu et al. proposed a new concept defined as $\dot{\kappa} = -\dot{Q}/(w\cdot\nabla T)$,where $\dot{Q}$ stands for heat energy, w is the width of the system, and ∇T is the temperature gradient. However, as stated by Wu et al., this new quantity $\dot{\kappa}$ named as "thermal sheet conductance" (W/K) is intrinsically different from the widely adopted definition of thermal conductivity κ (W/m·K) used by the academic thermal scientists. To keep consistent with previous studies, in this work, the vdW thickness values are adopted to calculate the in-plane thermal conductivities.

Simulations in this work are performed by the Large-scale Atomic/Molecular Massively Parallel Simulator (LAMMPS).[26] Periodic boundary conditions are used in the in-plane x and y directions to eliminate edge effects. Free boundary condition is applied in the out-of-plane z direction to allow the bilayer system to be fully relaxed. Structures of MoS_2 and $MoSe_2$ are shown in Figure 1. A small lattice mismatch of 2.5% is induced in the monolayers to achieve unified lattice constant. The initial distance between MoS_2 and $MoSe_2$ is set to 7.12 Å, which will be further adjusted upon equilibrium calculations. The final distance between MoS_2 and $MoSe_2$ equals 6.83 Å after structural relaxations. Atomic interactions within MoS_2 and $MoSe_2$ monolayers are described by the Stillinger−Weber potential,[27] which can be expressed as

$$\Phi(1, ..., N) = \sum_{i<j} V_2(r_{ij}) + \sum_{i<j<k} V_3(r_{ij}, r_{ik}, \theta_{ijk}) \quad (2)$$

The two-body V_2 and three-body V_3 interactions are written, respectively, as

$$V_2 = A\left(\frac{B}{r^p} - 1\right)\exp\left(\frac{\gamma}{r - r_{cut}}\right) \quad (3)$$

$$V_3 = K\exp\left(\frac{\gamma_1}{r_{ij} - r_0} + \frac{\gamma_2}{r_{jk} - r_1}\right)(\cos\theta - \cos\theta_0)^2 \quad (4)$$

where A, B, K, p, and γ are parameters to identify a reasonable choice of V_2 and V_3; r_{ij} and r_{jk} represent the atom distances between i, j and j, k.[28] The exponential functions provide a smooth and rapid decay of the interaction potential to zero and keep the potential short-range, which is important for efficient MD calculations. Parameter θ is the angle between two neighbor bonds and θ_0 stands for the equilibrium angle. Overall, the V_2 term describes the pairwise bond length variations and the V_3 term characterizes the neighboring bond angle variations. The van der Waals (vdW) interaction between MoS_2 and $MoSe_2$ is described by the 12−6 Lennard-Jones (LJ) potential

$$V(r) = 4\chi\varepsilon\left[\left(\frac{\sigma}{r}\right)^{12} - \left(\frac{\sigma}{r}\right)^{6}\right] \quad (5)$$

where σ is the distance parameter (Å), ε is the energy parameter (eV), and r is the interatomic distance. Parameter χ is used to adjust the interlayer coupling strength. The LJ parameters are taken from the universal force field (UFF) table.[29] Values of σ and ε for Se−S, Se−Mo, S−Mo, and Mo−Mo interactions are listed in Table 1. The cutoff distance for each pair interactions is set to 2.5σ. Time step is 0.5 fs (1 fs = 10^{-15} s) for all simulations.

Table 1. Lennard-Jones Parameters for MoS_2 and $MoSe_2$ vdW Interactions

	Se−S	Se−Mo	S−Mo	Mo−Mo
σ (Å)	3.670	3.192	3.126	2.719
ε (meV)	12.262	5.543	5.379	2.432

To calculate the interfacial thermal resistance between MoS_2 and $MoSe_2$, a transient pump−probe method is applied. This transient technique has been successfully used to investigate the thermal properties of graphene/Si,[30] graphene/boron-nitride,[31] phosphorene/Si,[32] and silicene/SiO_2.[33] After the MoS_2/$MoSe_2$ bilayer reaches steady state at equilibrium temperature, an ultrafast heat impulse of 50 fs is applied to one of the monolayers, for example, MoS_2. Upon the excitation, temperature of MoS_2 (T_{MoS_2}) will rise to a higher value, while the temperature of $MoSe_2$ (T_{MoSe_2}) remains unchanged. Because the only thermal pathway between the monolayers is interfacial thermal conduction, thermal energies accumulated in MoS_2 will quickly dissipate to $MoSe_2$ due to the temperature differences (ΔT). In the following thermal relaxation process, the total energy of MoS_2 (E_t) and temperature evolutions of MoS_2 and $MoSe_2$ are recorded at each time step. The classic definition of thermal resistance is expressed as $R = (T_1 - T_2)/\dot{q}$, where R is thermal resistance (K·m^2/W), T_1 and T_2 are the driven temperatures (K), and $\dot{q}$ is heat flux (W/m^2).[34] After the heat impulse, energy dissipation is through the heat conduction from MoS_2 to $MoSe_2$ until the system reaches thermal equilibrium again. Therefore, the transient heat flux is correlated to the energy variations in MoS_2 with time, which can be expressed as $\dot{q} = dE/(dt\cdot A)$, where A is the cross-sectional area based on the system's lateral dimensions. On the basis of the above discussions, interfacial thermal resistance can be calculated by

$$\frac{\partial E_t}{\partial t} = \frac{A\cdot(T_{MoSe_2} - T_{MoS_2})}{R} \quad (6)$$

The collected data points are averaged every 100 time steps to suppress data noise. The integral form $E_t = E_0 + (A/R)\cdot\int_0^t (T_{MoSe_2} - T_{MoS_2})\,dt$ is used for date fitting to find the optimum R value using the least-squares method. Symbol E_0 represents the initial energy. Correspondingly, when the thermal impulse is imposed on $MoSe_2$ instead of MoS_2, the interfacial thermal resistance can be calculated based on the energy of $MoSe_2$. In this work, thermal transport in both directions ($MoS_2 \leftrightarrow MoSe_2$) is investigated.

DOI: 10.1021/acs.jpcc.7b02547
J. Phys. Chem. C 2017, 121, 10336−10344

3. RESULTS AND DISCUSSION

To calculate the lateral thermal conductivity of the hybrid MoS_2−$MoSe_2$ system, a heterostructure with dimensions of 60.3 × 3.1 (x × y) nm^2 is created. Heat flux is applied in the length x direction from center to the edges. As shown in Figure 2a, the heat-source/heat-sink temperatures are controlled at T +ΔT and T−ΔT respectively, where ΔT equals 50 K. After the system reaches equilibrium at T = 300 K, temperatures of heat reservoirs at two ends are set at 250 K and the middle is set at 350 K. Temperature distributions of the system at steady state are shown in Figure 2b. It can be observed that there is a sharp temperature drop near the heating/cooling regions. Similar phenomena have been reported for various systems under NEMD simulations.[35−37] The nonlinear regions are caused by the fast kinetic and potential energy exchanges within the heat reservoirs and therefore should be excluded in the linear fitting. Temperature regions within the black brackets in Figure 2b are used for the ∇T calculations. The predicted ∇T for MoS_2, $MoSe_2$, and bilayer are 2.11, 2.19, and 2.18 K/nm, respectively. Temperature gradients are very close between individual monolayers with a 3.8% discrepancy. The accumulated thermal energies added/subtracted to heat reservoirs of MoS_2 and $MoSe_2$ are shown in Figure 2c. It is observed that the energy needed to maintain a 100 K temperature difference in MoS_2 is larger than that of $MoSe_2$, indicating that MoS_2 has higher thermal transport capability, which can dissipate thermal energies much faster from the heat source to the heat sinks. The slope of the energy profile can be used to determine the heat flux in each system. The calculated heat fluxes for MoS_2 and $MoSe_2$ are 0.742 and 0.478 eV/ps. Thermal conductivities of MoS_2 (κ_{MoS_2}), $MoSe_2$ (κ_{MoSe_2}), and bilayer (κ_b) are predicted to be 14.6, 8.6, and 11.4 W/m·K for the same system length of 60.3 nm, respectively. The calculated κ_{MoS_2} and κ_{MoSe_2} are very close to previous NEMD and equilibrium molecular dynamics (EMD) results.[19]

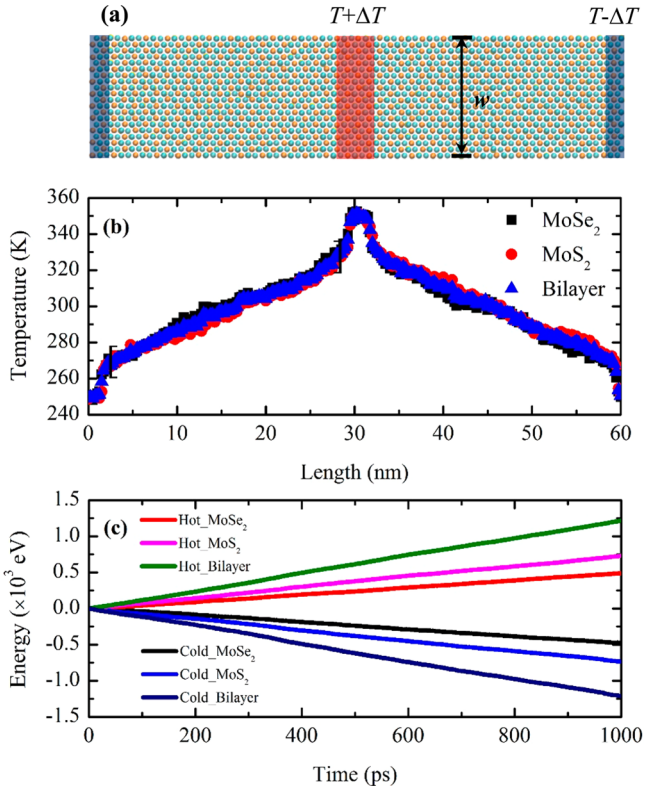

Figure 2. (a) Schematic of the NEMD setup on the heterostructure. Periodic boundary conditions are applied to the lateral directions and free boundary is used in the out-of-plane direction. (b) Temperature distributions in MoS_2, $MoSe_2$, and heterobilayer at steady state. (c) Aggregated energies added/subtracted in the heat reservoirs.

It is worth noting that classical MD simulations do not include any quantum effect, and all vibrational modes are excited regardless of temperature in the simulations. Some high-frequency modes are not excited when temperature is lower than Debye temperature. The Debye temperatures of MoS_2 and $MoSe_2$ are 262.3 and 177.6 K, respectively, based on first-principles calculations,[20] which is lower or around the MD temperatures used in this work. The low-frequency phonons that are the most important contributors to thermal transport are fully excited at this temperature range; therefore, quantum correction is not necessary. Besides, to make sure the system temperature distributions after NEMD calculations are still in linear response region, different values of ΔT are used to investigate the convergence of thermal conductivity on temperature difference. Aside from the above-mentioned ΔT = 50 K, other values of 20, 30, and 40 K are employed. The calculated thermal conductivities for a 14.1 × 3.1 (x × y) heterostructure with different ΔT are shown in Figure 3. The 14.1 × 3.1 (x × y) system is selected here to save computational cost. The temperature difference is denoted on the upper x axis, and corresponding κ values are shown on the left y axis. Each data point is averaged from three independent simulations with different initial conditions. The error bars represent the standard deviations of calculation. It can be observed that predicted thermal conductivities do not have noticeable variations with ΔT, indicating the validity of ΔT = 50 K.

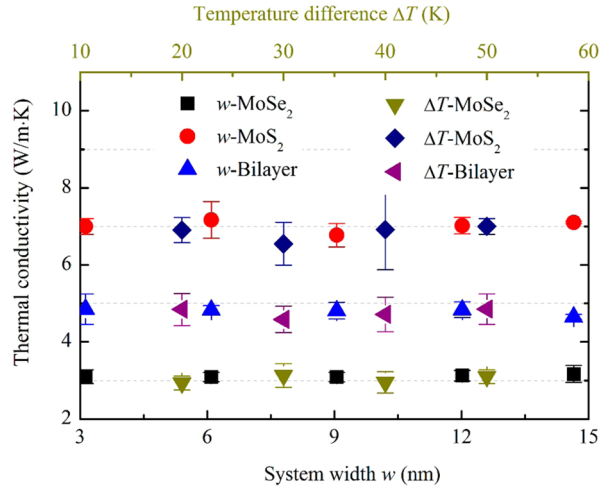

Figure 3. Variations of thermal conductivity κ with system width w and temperature difference ΔT. Illustrations of w and ΔT are shown in Figure 2a. The predicted κ is independent of w from 3 to 15 nm or ΔT from 20 to 50 K.

3.1. Effects of System Dimensions on Thermal Conductivity. The in-plane thermal conductivities calculated by NEMD method are dependent on system dimensions from two perspectives. First, similar to the EMD Green−Kubo method, when the sample size is too small, the Brillouin zone

DOI: 10.1021/acs.jpcc.7b02547
J. Phys. Chem. C 2017, 121, 10336−10344

has very coarse resolution, and the presented phonons are too few to reproduce the phonon−phonon scatterings in bulk materials. Because the system dimensions in NEMD simulations are, in general, much larger than those in EMD simulations, this effect can be safely neglected. However, because the width direction size (w) of the bilayer is much smaller than that of the length direction (l), convergence of thermal conductivity on w is investigated. Different w values of 3.1, 6.1, 9.1, 12.0, and 14.6 nm are used, and the calculated results are shown in Figure 3. Similar to the convergence study of ΔT, the same system length of 14.1 nm is used. System width is denoted on the bottom x axis, and corresponding κ values are shown on the left y axis. It shows that thermal conductivities do not change with enlarging w. Therefore, the smallest w value of 3.1 nm is chosen in this work for κ calculations to reduce the computational cost.

The other factor for the size-dependent thermal conductivity arises from the phonon scatterings at the sample/reservoir boundaries.[38] When the sample length is smaller than the phonon mean free path (MFP), thermal transport becomes ballistic, meaning certain phonon modes can transmit from the heat-source to heat-sink without scattering. The transport will gradually switch to diffusive when system length is increased. Because the ballistic thermal transport contributes less to the overall thermal conductivity due to their reduced MFP, the calculated κ results change with length on small scales. To address the length dependence of in-plane thermal conductivity, different lengths of 14.1, 30.0, 60.3, 120.1, 239.9, and 399.5 nm are used. The calculated κ results are shown in Figure 4a. It is observed that κ increases monotonically with system length and gradually converges at the highest length values. The calculated κ_{MoS_2}, κ_{MoSe_2}, and κ_b increase from 7.0, 3.1, and 4.8 W/m·K to 29.1, 19.5, and 24.0 W/m·K, respectively. The calculated thermal conductivity results are fitted using a linear function for lengths of 60.3−399.5 nm

$$\frac{1}{\kappa} = \frac{1}{\kappa_\infty}\left(\frac{2L}{l} + 1\right) \tag{7}$$

where L is effective phonon mean free path and κ_∞ is thermal conductivity for infinite length nanoribbon. The fitted results for $1/\kappa$ and $1/l$ are shown in Figure 4b. The predicted thermal conductivities for infinite-length MoS_2, $MoSe_2$, and bilayer are 32.9, 24.8, and 28.8 W/m·K, respectively. The calculated thermal conductivity of $MoS_2/MoSe_2$ 2D sheet is on the same order of magnitude with most TMDC materials.[20] The preserved in-plane thermal conductivity combined with its extraordinary electrical properties give this heterostructure advantageous positions in nanoelectronic and optoelectronic applications.

To gain a further insight into the different phonon behaviors of freestanding and supported monolayers, phonon spectral energy density (SED) is performed based on equation[39]

$$\phi(k, \omega) = \frac{1}{4\pi N\tau}\sum_{\alpha}\sum_{b}^{B} m_b \left| \int_0^\tau \sum_{n_{x,y,z}}^{N} \dot{v}_\alpha\begin{pmatrix} n_{x,y,z} \\ b \end{pmatrix}; t \exp\left[ik\cdot r\begin{pmatrix} n_{x,y,z} \\ 0 \end{pmatrix} - i\omega t\right] \mathrm{d}t \right|^2 \tag{8}$$

where N represents the number of total unit cells, τ is the integration time, α is the integration direction (x, y, z), B is the total number of atoms in a unit cell, $\dot{v}_\alpha$ is the velocity of atom b in unit cell $n_{x,y,z}$ at time step t, and r is the equilibrium position of unit cell $n_{x,y,z}$. The SED calculation is performed under NVE ensemble with an integration time step of 0.1 fs for a total simulation time of 100 ps. The unit-cell length a is 3.292 Å. The calculated SED results for freestanding and supported $MoSe_2$ are shown in Figure 5a,b, respectively. It can be observed that the flexural phonon mode in $MoSe_2$ at k_0 point shifted to a higher frequency in the bilayer structure. Similar results have also been observed in silicene,[40] graphene,[41] and

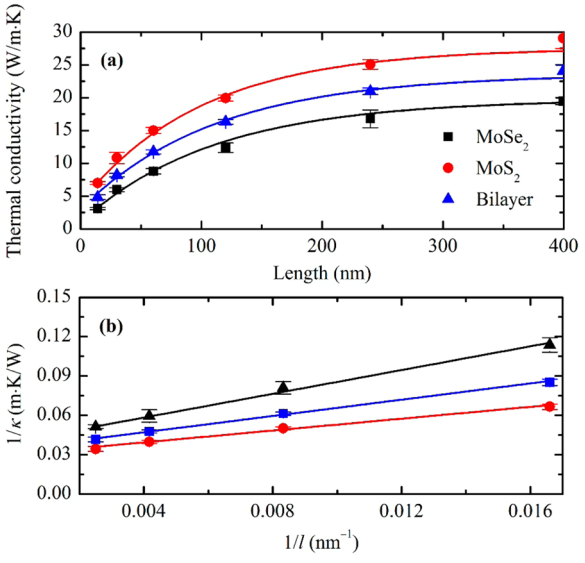

Figure 4. (a) Dependence of thermal conductivity with system length l. The predicted thermal conductivity increases monotonically with system length and gradually converges at the highest length values. (b) Inverse correlations between $1/\kappa$ and $1/l$. Bulk thermal conductivities are extracted based on the linear fitting profiles. Coupling strength χ equals 1. Each data point is averaged from three independent simulations with different initial conditions.

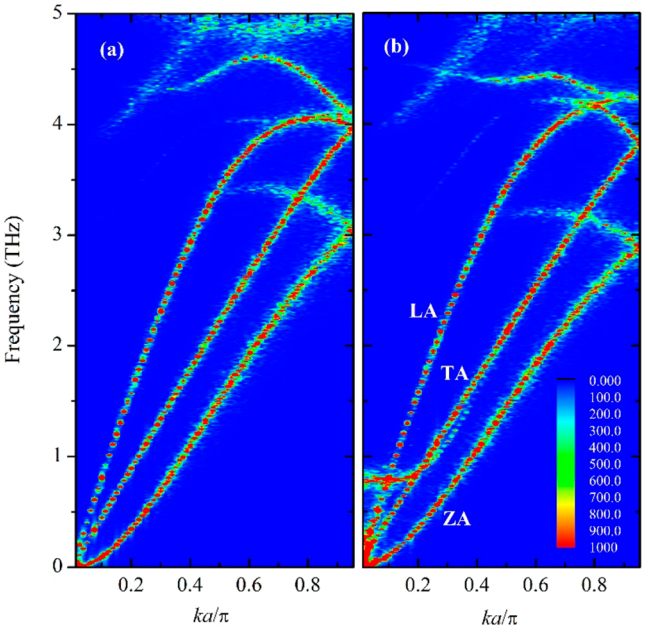

Figure 5. Phonon spectral energy densities of (a) freestanding $MoSe_2$ and (b) supported $MoSe_2$ in $MoSe_2/MoS_2$ bilayer. The shading areas indicate the SED magnitude for 2D Fourier transform of each k and f combination with an integration time of 100 ps.

DOI: 10.1021/acs.jpcc.7b02547
J. Phys. Chem. C 2017, 121, 10336−10344

hexagonal boron nitride.[42] The variation is mainly attributed to the restricted phase space for phonon−phonon scattering in the out-of-plane direction and the weak vdW interactions between $MoSe_2$ and MoS_2, which could modify the interatomic force constants of $MoSe_2$. The SED differences shed some light on the discrepancies of phonon thermal transport in freestanding and supported $MoSe_2$.

3.2. Effects of Temperature and Coupling Strength. Thermal interface materials are often placed under extreme working environments with a wide range of ambient conditions. The most relevant environmental variables are temperature and contact pressure, which could directly affect the device's thermal performances and cause adverse effects on structural stability. Therefore, effects of system temperature and coupling strength on in-plane thermal conductivity are investigated. A bilayer system of 30.0×3.1 $(x \times y)$ nm^2 is selected for both the temperature and coupling strength studies. Different system temperatures of 100, 200, 300, 400, and 500 K are applied and the calculated κ results are shown in Figure 6. It is observed

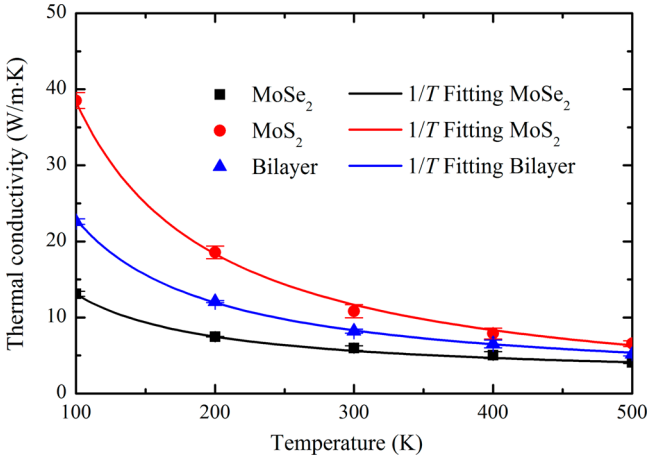

Figure 6. Temperature dependence of thermal conductivity from 100 to 500 K. The inverse relationship between thermal conductivity and temperature ($\kappa \approx 1/T$) indicates the Umklapp scattering is dominant at this temperature range. Coupling strength χ equals 1. Each data point is averaged from three independent simulations with different initial conditions.

that thermal conductivities of both MoS_2 and $MoSe_2$ decrease monotonically with temperature, which is as expected for phonon dominated crystalline materials. As the system temperature is increased, higher frequency phonons become activated and the phonon population grows. As a result, the Umklapp phonon scattering becomes more severe, which directly reduces thermal conductivity in the 2D sheet. The maximum κ reduction of MoS_2, $MoSe_2$, and bilayers are calculated as 83.0, 68.9, and 77.1%, respectively. Similar results have been reported by Taube et al.[43] using Raman method. The measured thermal conductivity of supported MoS_2 decreases from 62.2 W/m·K at 300 K to 7.45 W/m·K at 450 K. The decreasing trend of thermal conductivity has also been confirmed for few-layer MoS_2 structures using a microbridge method.[44] The calculated thermal conductivity results are fitted with an inverse relationship with temperature ($\kappa \approx 1/T$). It can be observed that the fitting curves soundly match the calculated thermal conductivities, indicating that the Umklapp scattering is dominant at this temperature range.[45]

Effects of coupling strength on in-plane thermal conductivity is investigated by altering the LJ potential coupling strength χ to different values of 0.5, 1.0, 2.0, 3.0, and 4.0. The calculated thermal conductivities are plotted against χ in Figure 7. Each

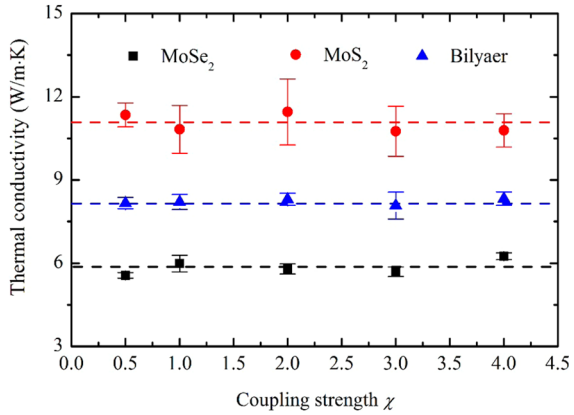

Figure 7. Dependence of thermal conductivity with interlayer coupling strength χ. The calculated thermal conductivity has negligible changes with coupling strength.

data point is averaged from three independent simulations with different initial conditions. It shows that thermal conductivity has negligible changes with coupling strength, suggesting that the basal-plane thermal performance of $MoS_2/MoSe_2$ bilayer will not be affected by interfacial interactions. To gain further insights about the effect of coupling strength on phonon behaviors, phonon power spectra of MoS_2 and $MoSe_2$ in the heterostructure are calculated, respectively, for all χ values. The phonon power spectra can be calculated by taking the Fourier transform of the velocity autocorrelation function (VACF)

$$G(\omega) = \frac{1}{\sqrt{2\pi}} \int_{-\infty}^{\infty} <v(0)\cdot v(t)> / <v(0)\cdot v(0)> e^{i\omega t}\, dt \quad (9)$$

where v is atom velocity and the angle brackets mean ensemble averaging. The calculated velocity densities of state (VDOSs) are shown in Figure 8. It is shown that for both MoS_2 and $MoSe_2$, the VDOSs are softened with increasing χ. However, the peak locations remain unchanged in all cases, indicating that the group velocities are not affected by coupling strength.

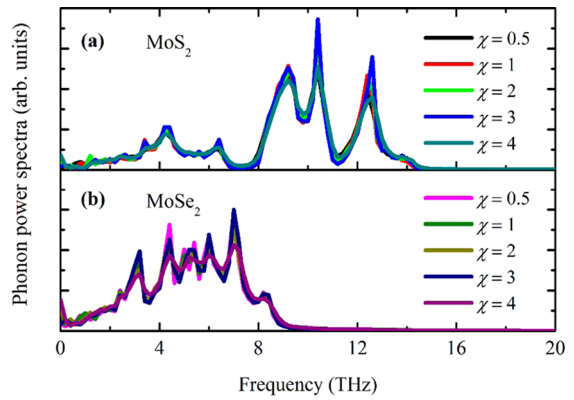

Figure 8. Phonon power spectra of (a) MoS_2 and (b) $MoSe_2$ with interlayer coupling strength χ. The calculated VDOS are softened with increasing χ, while the peak locations remain unchanged.

DOI: 10.1021/acs.jpcc.7b02547
J. Phys. Chem. C 2017, 121, 10336−10344

3.3. Out-of-Plane Thermal Conductance. Out-of-plane thermal conductance also plays a vital role in heat dissipations. Using a refined optothermal Raman technique, interfacial thermal resistance (R) between MoS_2/Au and $MoSe_2/SiO_2$ is characterized as 2.3×10^{-6} K·m^2/W and 1.1×10^{-5} K·m^2/W, respectively.[46] On the basis of Raman spectroscopy method, Yuan et al.[47] reported thickness-dependent interfacial thermal resistance between MoS_2 and crystalline silicon. The measured R decreases from 1.03×10^{-6} to 1.46×10^{-8} K·m^2/W with increasing MoS_2 layer numbers. The reduced R value reveals their better interface contact with substrate, leading to accordingly improved interfacial energy coupling. Despite the above-mentioned investigations on interfacial thermal conductance between $MoS_2/MoSe_2$ and substrates, however, the R value within MoS_2 and $MoSe_2$ bilayer has not yet been explored. In this work, the interfacial thermal resistance between MoS_2 and $MoSe_2$ is calculated using the transient pump−probe method. Lateral dimensions of the heterostructure are 14.1×14.6 ($x \times y$) nm^2. Periodic boundary conditions are applied in x and y directions and free boundary condition is used in the out-of-plane z direction. After the system reaches thermal equilibrium at temperature 300 K, a thermal impulse of 6×10^{12} W/m^2 is applied to the $MoSe_2$ monolayer continuously for 50 fs. Upon the release of the excitation, T_{MoSe_2} increases to ~520 K, while T_{MoS_2} remains at 300 K. In the following thermal relaxation process, system energy (E_t) of $MoSe_2$, T_{MoSe_2}, and T_{MoSe_2} is recorded at each time step for 1000 ps. Temperature and energy evolutions of the system are shown in Figure 9a,b separately. On the basis of eq 6, the interfacial

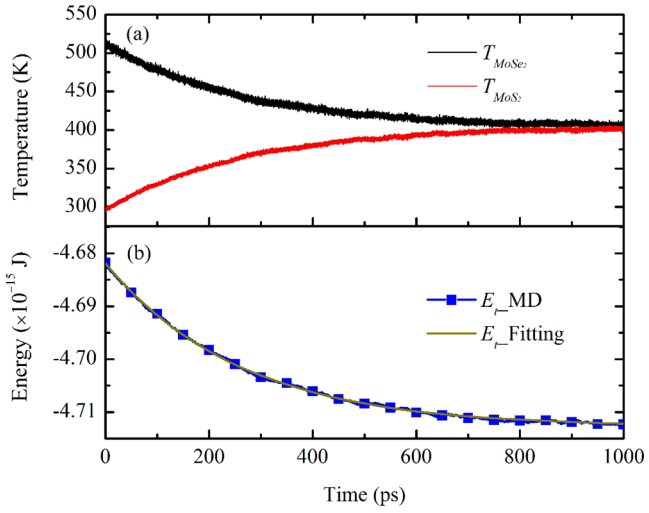

Figure 9. (a) Temperature evolutions of MoS_2 and $MoSe_2$ after 50 fs heat impulse. (b) Energy profile of $MoSe_2$ and its fitting curve during thermal relaxation.

thermal resistance can be calculated by best-fitting the energy profiles. It can be observed in Figure 9b that the fitting curve soundly matches the MD result, indicating the validity of the predicted value.

Aside from the $MoSe_2 \rightarrow MoS_2$ thermal transport, interfacial thermal resistance in the reverse direction $MoS_2 \rightarrow MoSe_2$ is also calculated. The predicted results from temperature of 100 to 500 K are shown in Figure 10. Each data point is averaged from five independent simulations with different initial conditions. The error bars represent standard deviations. Two

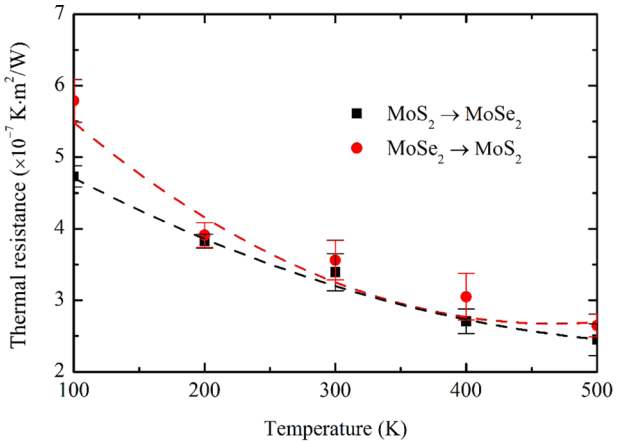

Figure 10. Interfacial thermal resistance predicted from temperatures of 100 to 500 K with heat flux in both directions between MoS_2 and $MoSe_2$. The heat flow runs preferably from MoS_2 to $MoSe_2$ than in the reverse direction.

phenomena are observed from the calculated results. First, the predicted thermal resistance decreases with increasing temperature in both directions. Second, R of $MoS_2 \rightarrow MoSe_2$ is slightly lower than that of $MoSe_2 \rightarrow MoS_2$, indicating that the heat flow runs preferably from MoS_2 to $MoSe_2$ than in the reverse direction. For example, at temperature 300 K, R of $MoS_2 \rightarrow$ MoSe2 and $MoSe_2 \rightarrow MoS_2$ equal 3.39×10^{-7} and 3.56×10^{-7} K·m^2/W, respectively. It has been proven that at vdW heterojunctions, inelastic scattering provides the major contribution to the energy transport, surpassing that of elastic scattering at high temperatures.[48] The increased probability of inelastic scattering is due to the fact that at high temperature, the high-frequency phonons might break down into large volumes of low-frequency phonons. These low-frequency phonons have higher probability being transferred through an interface when compared with the high-frequency phonons, leading to higher phonon transmission coefficients and lowered interfacial thermal resistance for the system with increased temperature. Wu et al.[49] investigated the role of anharmonicity in the thermal transport across a model interface consisting of a monatomic lattice and a diatomic lattice. It is found that the anharmonicity inside a material plays an important role in interfacial thermal transport by facilitating the energy communication between different phonon modes. The anharmonicity at the interface has much less impact on the interfacial thermal transport. The stronger anharmonic scattering at higher temperatures leads to more energy redistribution to low-frequency phonons, which can transfer heat across the interface more efficiently.

4. CONCLUSIONS

The in-plane thermal conductivity and out-of-plane thermal conductance between two popular TMDC materials, MoS_2 and $MoSe_2$, are systematically investigated. The predicted κ for infinite length $MoS_2/MoSe_2$ heterostructure equals 28.8 W/m·K at room temperature, which preserves the high thermal conductivity of MoS_2 and $MoSe_2$ monolayers and gives it advantageous positions in nanoelectronic and optoelectronic applications. System temperature is found to dramatically decrease the calculated lateral thermal conductivity, leading to maximum κ reductions amounting to 83.0, 68.9, and 77.1%, respectively, for MoS_2, $MoSe_2$, and bilayer. On the contrary, the

DOI: 10.1021/acs.jpcc.7b02547
J. Phys. Chem. C 2017, 121, 10336−10344

increased temperature could facilitate the out-of-plane thermal conductance by reducing the interfacial thermal resistance values. Moreover, the calculated thermal conductivity of MoS_2/$MoSe_2$ bilayer does not change with coupling strengths, which is beneficial to pliable heterostructures because the thermal performance will not be affected by contact pressure alterations. These results not only shed light on the phonon transport mechanisms within MoS_2/$MoSe_2$ heterostructures but also provide guidelines for the design and optimization of such interfaces for thermal management in TMDC-based electronic devices.

AUTHOR INFORMATION

Corresponding Authors

*J.Z.: E-mail: zhang@unl.edu.

*Y.Y.: E-mail: yyue@whu.edu.cn.

ORCID

Jingchao Zhang: 0000-0001-5289-6062

Notes

The authors declare no competing financial interest.

ACKNOWLEDGMENTS

Support of this work from Holland Computing Center of the University of Nebraska-Lincoln and National Natural Science Foundation of China (Nos. 51576145, 51376140, 51279145, and 51566012) is greatly appreciated.

REFERENCES

(1) Ohno, Y.; Young, D. K.; Beschoten, B.; Matsukura, F.; Ohno, H.; Awschalom, D. D. Electrical Spin Injection in a Ferromagnetic Semiconductor Heterostructure. *Nature* **1999**, *402*, 790−792.

(2) Koma, A. Van Der Waals Epitaxy for Highly Lattice-Mismatched Systems. *J. Cryst. Growth* **1999**, *201*−*202*, 236−241.

(3) Sorkin, V.; Pan, H.; Shi, H.; Quek, S. Y.; Zhang, Y. W. Nanoscale Transition Metal Dichalcogenides: Structures, Properties, and Applications. *Crit. Rev. Solid State Mater. Sci.* **2014**, *39*, 319−367.

(4) Zhang, K.; Lin, Y. C.; Robinson, J. A. Synthesis, Properties, and Stacking of Two-Dimensional Transition Metal Dichalcogenides. *Semicond. Semimetals* **2016**, *95*, 189−219.

(5) Chen, X.; McDonald, A. R. Functionalization of Two-Dimensional Transition-Metal Dichalcogenides. *Adv. Mater.* **2016**, *28*, 5738−5746.

(6) Ma, J. L.; Li, W.; Luo, X. B. Ballistic Thermal Transport in Monolayer Transition-Metal Dichalcogenides: Role of Atomic Mass. *Appl. Phys. Lett.* **2016**, *108*, 082102.

(7) Splendiani, A.; Sun, L.; Zhang, Y.; Li, T.; Kim, J.; Chim, C.-Y.; Galli, G.; Wang, F. Emerging Photoluminescence in Monolayer Mos2. *Nano Lett.* **2010**, *10*, 1271−1275.

(8) Mak, K. F.; Lee, C.; Hone, J.; Shan, J.; Heinz, T. F. Atomically Thin Mos 2: A New Direct-Gap Semiconductor. *Phys. Rev. Lett.* **2010**, *105*, 136805.

(9) Zhang, Y.; Chang, T.-R.; Zhou, B.; Cui, Y.-T.; Yan, H.; Liu, Z.; Schmitt, F.; Lee, J.; Moore, R.; Chen, Y.; et al. Direct Observation of the Transition from Indirect to Direct Bandgap in Atomically Thin Epitaxial Mose2. *Nat. Nanotechnol.* **2013**, *9*, 111−115.

(10) Lu, N.; Guo, H.; Li, L.; Dai, J.; Wang, L.; Mei, W.-N.; Wu, X.; Zeng, X. C. Mos2/Mx2 Heterobilayers: Bandgap Engineering Via Tensile Strain or External Electrical Field. *Nanoscale* **2014**, *6*, 2879−2886.

(11) He, J.; Hummer, K.; Franchini, C. Stacking Effects on the Electronic and Optical Properties of Bilayer Transition Metal Dichalcogenides Mos2, Mose2, Ws2, and Wse2. *Phys. Rev. B: Condens. Matter Mater. Phys.* **2014**, *89*, 075409.

(12) Gong, Y.; et al. Vertical and in-Plane Heterostructures from Ws2/Mos2Monolayers. *Nat. Mater.* **2014**, *13*, 1135−1142.

(13) He, X.; Li, H.; Zhu, Z.; Dai, Z.; Yang, Y.; Yang, P.; Zhang, Q.; Li, P.; Schwingenschlogl, U.; Zhang, X. Strain Engineering in Monolayer Ws2, Mos2, and the Ws2/Mos2 Heterostructure. *Appl. Phys. Lett.* **2016**, *109*, 173105.

(14) Son, Y.; Li, M.-Y.; Cheng, C.-C.; Wei, K.-H.; Liu, P.; Wang, Q. H.; Li, L.-J.; Strano, M. S. Observation of Switchable Photoresponse of a Monolayer Wse2−Mos2 Lateral Heterostructure Via Photocurrent Spectral Atomic Force Microscopic Imaging. *Nano Lett.* **2016**, *16*, 3571−3577.

(15) Ma, Z.; Hu, Z.; Zhao, X.; Tang, Q.; Wu, D.; Zhou, Z.; Zhang, L. Tunable Band Structures of Heterostructured Bilayers with Transition-Metal Dichalcogenide and Mxene Monolayer. *J. Phys. Chem. C* **2014**, *118*, 5593−5599.

(16) Tang, Q.; Zhou, Z.; Chen, Z. Innovation and Discovery of Graphene-Like Materials Via Density-Functional Theory Computations. *Wiley Interdisciplinary Reviews: Computational Molecular Science* **2015**, *5*, 360−379.

(17) Yan, R.; Simpson, J. R.; Bertolazzi, S.; Brivio, J.; Watson, M.; Wu, X.; Kis, A.; Luo, T.; Hight Walker, A. R.; Xing, H. G. Thermal Conductivity of Monolayer Molybdenum Disulfide Obtained from Temperature-Dependent Raman Spectroscopy. *ACS Nano* **2014**, *8*, 986−993.

(18) Gandi, A. N.; Schwingenschlögl, U. Thermal conductivity of bulk and monolayer MoS_2. *EPL (Europhysics Letters)* **2016**, *113*, 36002.

(19) Hong, Y.; Zhang, J.; Zeng, X. C. Thermal Conductivity of Monolayer Mose2 and Mos2. *J. Phys. Chem. C* **2016**, *120*, 26067−26075.

(20) Peng, B.; Zhang, H.; Shao, H.; Xu, Y.; Zhang, X.; Zhu, H. Thermal Conductivity of Monolayer Mos2, Mose2, and Ws2: Interplay of Mass Effect, Interatomic Bonding and Anharmonicity. *RSC Adv.* **2016**, *6*, 5767−5773.

(21) Schneider, T.; Stoll, E. Molecular-Dynamics Study of a Three-Dimensional One-Component Model for Distortive Phase Transitions. *Phys. Rev. B: Condens. Matter Mater. Phys.* **1978**, *17*, 1302−1322.

(22) Zhang, J.; Wang, X. Thermal Transport in Bent Graphene Nanoribbons. *Nanoscale* **2013**, *5*, 734−743.

(23) Zhang, J.; Wang, X.; Xie, H. Phonon Energy Inversion in Graphene During Transient Thermal Transport. *Phys. Lett. A* **2013**, *377*, 721−726.

(24) Zhang, J.; Wang, X.; Xie, H. Co-Existing Heat Currents in Opposite Directions in Graphene Nanoribbons. *Phys. Lett. A* **2013**, *377*, 2970−2978.

(25) Wu, X.; Varshney, V.; Lee, J.; Pang, Y.; Roy, A. K.; Luo, T. How to Characterize Thermal Transport Capability of 2d Materials Fairly? − Sheet Thermal Conductance and the Choice of Thickness. *Chem. Phys. Lett.* **2017**, *669*, 233−237.

(26) Plimpton, S. Fast Parallel Algorithms for Short-Range Molecular Dynamics. *J. Comput. Phys.* **1995**, *117*, 1−19.

(27) Kandemir, A.; Yapicioglu, H.; Kinaci, A.; Çağın, T.; Sevik, C. Thermal transport properties of MoS_2 and $MoSe_2$ monolayers. *Nanotechnology* **2016**, *27*, 055703.

(28) Stillinger, F. H.; Weber, T. A. Computer Simulation of Local Order in Condensed Phases of Silicon. *Phys. Rev. B: Condens. Matter Mater. Phys.* **1985**, *31*, 5262−5271.

(29) Rappe, A. K.; Casewit, C. J.; Colwell, K. S.; Goddard, W. A.; Skiff, W. M. Uff, a Full Periodic Table Force Field for Molecular Mechanics and Molecular Dynamics Simulations. *J. Am. Chem. Soc.* **1992**, *114*, 10024−10035.

(30) Zhang, J.; Wang, Y.; Wang, X. Rough Contact Is Not Always Bad for Interfacial Energy Coupling. *Nanoscale* **2013**, *5*, 11598−11603.

(31) Zhang, J.; Hong, Y.; Yue, Y. Thermal Transport across Graphene and Single Layer Hexagonal Boron Nitride. *J. Appl. Phys.* **2015**, *117*, 134307.

(32) Zhang, J.; Hong, Y.; Liu, M.; Yue, Y.; Xiong, Q.; Lorenzini, G. Molecular Dynamics Simulation of the Interfacial Thermal Resistance between Phosphorene and Silicon Substrate. *Int. J. Heat Mass Transfer* **2017**, *104*, 871−877.

DOI: 10.1021/acs.jpcc.7b02547
J. Phys. Chem. C 2017, 121, 10336−10344

(33) Zhang, J.; Hong, Y.; Tong, Z.; Xiao, Z.; Bao, H.; Yue, Y. Molecular Dynamics Study of Interfacial Thermal Transport between Silicene and Substrates. *Phys. Chem. Chem. Phys.* **2015**, *17*, 23704−23710.
(34) Incropera, F. P. *Fundamentals of Heat and Mass Transfer*, 6th ed.; John Wiley: Hoboken, NJ, 2007; p *xxv*, 997 p.
(35) Zhang, X.; Bao, H.; Hu, M. Bilateral Substrate Effect on the Thermal Conductivity of Two-Dimensional Silicon. *Nanoscale* **2015**, *7*, 6014−6022.
(36) Chen, W.; Zhang, J.; Yue, Y. Molecular Dynamics Study on Thermal Transport at Carbon Nanotube Interface Junctions: Effects of Mechanical Force and Chemical Functionalization. *Int. J. Heat Mass Transfer* **2016**, *103*, 1058−1064.
(37) Zhang, Y.-Y.; Pei, Q.-X.; Mai, Y.-W.; Lai, S.-K. Interfacial Thermal Conductance in Multilayer Graphene/Phosphorene Heterostructure. *J. Phys. D: Appl. Phys.* **2016**, *49*, 465301.
(38) Sellan, D. P.; Landry, E. S.; Turney, J. E.; McGaughey, A. J. H.; Amon, C. H. Size Effects in Molecular Dynamics Thermal Conductivity Predictions. *Phys. Rev. B: Condens. Matter Mater. Phys.* **2010**, *81*, 214305.
(39) Thomas, J. A.; Turney, J. E.; Iutzi, R. M.; Amon, C. H.; McGaughey, A. J. H. Predicting Phonon Dispersion Relations and Lifetimes from the Spectral Energy Density. *Phys. Rev. B: Condens. Matter Mater. Phys.* **2010**, *81*, 081411.
(40) Wang, Z.; Feng, T.; Ruan, X. Thermal Conductivity and Spectral Phonon Properties of Freestanding and Supported Silicene. *J. Appl. Phys.* **2015**, *117*, 084317.
(41) Xu, W.; Zhang, G.; Li, B. Interfacial Thermal Resistance and Thermal Rectification between Suspended and Encased Single Layer Graphene. *J. Appl. Phys.* **2014**, *116*, 134303.
(42) Zhang, J.; Wang, X.; Hong, Y.; Xiong, Q.; Jiang, J.; Yue, Y. Understanding Thermal Transport in Asymmetric Layer Hexagonal Boron Nitride Heterostructure. *Nanotechnology* **2017**, *28*, 035404.
(43) Taube, A.; Judek, J.; Łapińska, A.; Zdrojek, M. Temperature-Dependent Thermal Properties of Supported Mos2Monolayers. *ACS Appl. Mater. Interfaces* **2015**, *7*, 5061−5065.
(44) Jo, I.; Pettes, M. T.; Ou, E.; Wu, W.; Shi, L. Basal-Plane Thermal Conductivity of Few-Layer Molybdenum Disulfide. *Appl. Phys. Lett.* **2014**, *104*, 201902.
(45) Tritt, T. M. *Thermal Conductivity: Theory, Properties, and Applications*; Kluwer Academic/Plenum Publishers: New York, 2004; p *xxi*, 290 p.
(46) Zhang, X.; Sun, D.; Li, Y.; Lee, G.-H.; Cui, X.; Chenet, D.; You, Y.; Heinz, T. F.; Hone, J. C. Measurement of Lateral and Interfacial Thermal Conductivity of Single- and Bilayer Mos2 and Mose2 Using Refined Optothermal Raman Technique. *ACS Appl. Mater. Interfaces* **2015**, *7*, 25923−25929.
(47) Yuan, P.; Li, C.; Xu, S.; Liu, J.; Wang, X. Interfacial Thermal Conductance between Few to Tens of Layered-Mos2 and C-Si: Effect of Mos2 Thickness. *Acta Mater.* **2017**, *122*, 152−165.
(48) Stevens, R. J.; Zhigilei, L. V.; Norris, P. M. Effects of Temperature and Disorder on Thermal Boundary Conductance at Solid−Solid Interfaces: Nonequilibrium Molecular Dynamics Simulations. *Int. J. Heat Mass Transfer* **2007**, *50*, 3977−3989.
(49) Wu, X.; Luo, T. The Importance of Anharmonicity in Thermal Transport across Solid-Solid Interfaces. *J. Appl. Phys.* **2014**, *115*, 014901.

DOI: 10.1021/acs.jpcc.7b02547
J. Phys. Chem. C 2017, 121, 10336−10344